

Dynamics of anchored oscillating nanomenisci

Caroline Mortagne,^{1,2} Kevin Lippera,^{1,3} Philippe Tordjeman,² Michael Benzaquen,³ and Thierry Ondarçuhu¹

¹CEMES-CNRS, UPR 8011, 29 rue Jeanne Marvig, 31055 Toulouse Cedex 4, France

²IMFT - Université de Toulouse, CNRS-INPT-UPS, UMR 5502,

1 allée du Professeur Camille Soula, 31400 Toulouse, France

³LadHyX - UMR CNRS 7646, École Polytechnique,
Boulevard des Maréchaux, 91120 Palaiseau, France

(Dated: April 20, 2022)

We present a self-contained study of the dynamics of oscillating nanomenisci anchored on nanometric topographical defects around a cylindrical nanofiber – radius below 100 nm. Using frequency-modulation atomic force microscopy (FM-AFM), we show that the friction coefficient surges as the contact angle is decreased. We propose a theoretical model within the lubrication approximation that reproduces the experimental data and provides a comprehensive description of the dynamics of the nanomeniscus. The dissipation pattern in the vicinity of the contact line and the anchoring properties are discussed as a function of liquid and surface properties in addition to the solicitation conditions.

The study of liquid dynamics in the close vicinity of the contact line is fundamental to understand the physics of wetting [1, 2]. The strong confinement inherent to this region leads, in the case of a moving contact line, to a divergence of the energy dissipation. This singularity can be released by the introduction of microscopic models based on long range interactions, wall slippage or diffuse interface [3] which are still difficult to determine experimentally. In most cases, the spreading is also controlled by the pinning of the contact line on surface defects [4, 5]. For nanometric defects, the intensity and localisation of the viscous energy dissipation is an open issue to understand the wetting dynamics. The aim of this paper is to study the hydrodynamics of a nanomeniscus anchored on nanometric topographic defects and subjected to an external periodic forcing. In addition to wetting dynamics on rough surfaces, this issue is relevant for vibrated droplets or bubbles [6] and for the reflection of capillary waves on a solid wall [7].

Atomic force microscopy (AFM) has proven to be a unique tool to carry out measurements on liquids down to the nanometer scale: liquid structuration [8] or slippage [9] at solid interfaces were evidenced, while the use of specific tips fitted with either micro- or nano- cylinders allowed quantitative measurements in viscous boundary layers [10] and at the contact line [11]. In this study, we have developed an AFM experiment based on the Frequency Modulation mode (FM-AFM) to monitor, simultaneously, the mean force and the energy dissipation experienced by an anchored nanomeniscus. Artificial defects with adjustable size are deposited on cylindrical fibers (radius 100 nm) to control the pinning of the contact line and the meniscus stretching during the oscillation. The experiments are analyzed in the frame of a nanohydrodynamics model based on the lubrication approximation. Interestingly, the meniscus oscillation does not lead to any stress divergence at the contact line allowing a full resolution without the use of cutoff lengths.

This study thus provides a comprehensive description of dissipation mechanisms in highly confined menisci and an estimate of the critical depinning contact angle for nanometric defects.

The fibres used in the experimental study were carved with a dual beam FIB (1540 XB Cross Beam, Zeiss) from conventional silicon AFM probes (OLTESPA, Bruker). Using a beam of Ga ions, a 2 to 3- μm long cylinder of radius $R \sim 80$ nm is milled at the end of a classical AFM tip. An ELPHY MultiBeam (Raith) device allows to manufacture nanometric spots of platinum by Electron Beam Induced Deposition (EBID) in order to cre-

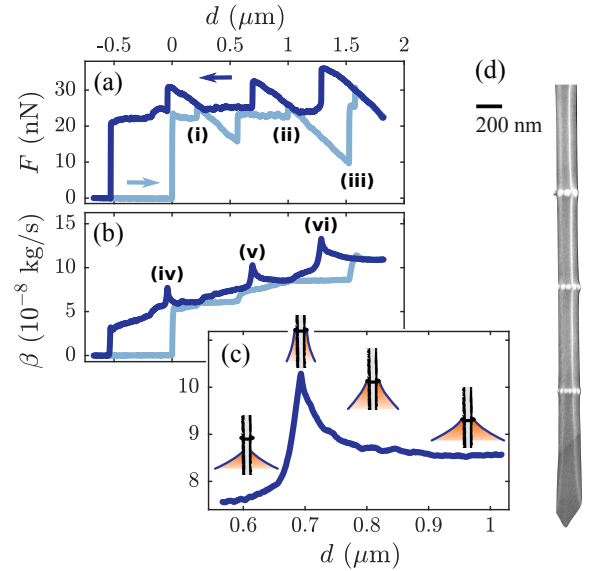


FIG. 1. FM-AFM spectroscopy curves performed on a 3EG liquid drop. (a) Force F and (b) friction coefficient β as a function of the immersion depth d . (c) Zoom on the friction coefficient curve on the second defect with sketches of the meniscus. (d) SEM image of the 3.2 μm long and 170 nm diameter probe, covered by three platinum rings of thicknesses $r_0 = 10, 15$ and 40 nm, from bottom to top respectively.

ate ring defect of controlled thickness around the cylinders (see Supplemental Material SM). An example of a home-made cylinder with three annular rings is displayed in Fig. 1.(d). The liquids used are ethylene glycol (1EG), diethylene glycol (2EG), triethylene glycol (3EG) and an ionic liquid, namely 1-ethyl-3-methylimidazolium tetrafluoroborate (IL). The liquids have a low volatility at room temperature. Their dynamic viscosities are $\eta = 19.5, 34.5, 46.5$ and 44 mPa.s and their surface tensions are $\gamma = 49.5, 49.5, 48$ and 56 mN.m at 20°C , respectively. As surface conditions play a crucial role in wetting, measurements are made before and after a five minutes UV/O₃ treatment aimed at removing contaminants and making the surface more hydrophilic [12].

Using a PicoForce AFM (Bruker), the tips are dipped in and withdrawn from a millimetric liquid drop deposited on a silicon substrate. The experiments are performed in Frequency Modulation (FM-AFM) mode using a phase-lock loop device (HF2LI, Zurich Instrument) which oscillates the cantilever at its resonance frequency. A PID controller is used to maintain the oscillation amplitude A constant. The excitation signal A_{ex} is linearly related to the friction coefficient of the interaction [13] through $\beta = \beta_0 (A_{\text{ex}}/A_{\text{ex},0} - 1)$, where $A_{\text{ex},0}$ and β_0 are respectively the excitation signal and the friction coefficient of the free system in air. Since we used cantilevers with high quality factor $Q \sim 200$ the resonant frequency coincides with the natural angular frequency $\omega_0 = 2\pi f$, and thus $\beta_0 = k/(\omega_0 Q)$ where k is the cantilever stiffness. The force is obtained as $F = k\bar{\delta}$ where $\bar{\delta}$ is the mean deflection during the oscillation.

Figure 1 shows the results of a typical experiment performed on a 3EG drop. The measured force F [Fig. 1.(a)] and friction coefficient β [Fig. 1.(b)] are plotted as a function of the immersion depth d for a ramp of $2.5 \mu\text{m}$. The cylinder is dipped in (light blue curves) and withdrawn (dark blue curves) from the liquid bath at $2.5 \mu\text{m.s}^{-1}$. The tip oscillates at its resonance frequency (66 820 Hz in air) with an amplitude of 6 nm. The cantilever stiffness is $k = 1.5 \text{ N.m}^{-1}$, soft enough to perform deflection measurements while being adapted for the dynamic mode. The force curve can be interpreted using the expression of the capillary force [14]: $F = 2\pi R\gamma \cos \bar{\theta}$, where R is the fiber radius and $\bar{\theta}$ is the mean contact angle during the oscillation. After the meniscus formation at $d = 0$, and until the contact line anchors on the first ring (at reference (i)) F and $\bar{\theta}$ remain constant, consistent with [14–16]. A small jump of the force is observed when the contact line reaches a platinum ring on reference points (i), (ii) or (iii). Once the meniscus is pinned, the contact angle increases as the cylinder goes deeper into the liquid, leading to a decrease of the force F . Conversely, the withdrawal leads to a decrease of $\bar{\theta}$ and an increase of the force F on the left of (i), (ii) and (iii). Hence, each ring induces two hysteresis cycles characteristic of strong topographic defects [4].

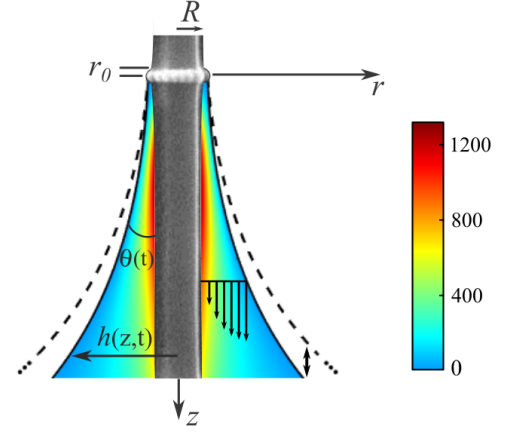


FIG. 2. Oscillating meniscus anchored on a defect, displayed in the frame of reference of the fibre. The velocity profile (black arrows) is calculated from Eq. (4). The stress field $\eta \partial_r v$ (color gradient) is computed for $R=100$ nm, $r_0 = 30$ nm, $l_c=2$ mm, $A=10$ nm, $f = 65$ kHz, $\theta_e = 10^\circ$ and $\eta = 30$ mPa.s. Colorbar in Pa.

Different contributions to the probe-liquid system account for the friction coefficient behavior. The global increase of β with d observed on Fig. 1(b) results from the contribution of the viscous layer around the tip which is proportional to the immersion depth [10]. At withdrawal, β increases dramatically when the probe reaches the reference points (iv), (v) and (vi) of Fig. 1(b). In those regions, the force curve indicates that the meniscus is pinned on a defect. The dissipation growth is therefore attributed to the decrease of the contact angle before de-pinning as schematized on the zoom on the friction coefficient curve [Fig. 1(c)]. This large effect can be qualitatively understood considering that small contact angles – corresponding to reduced film thickness – generate strong velocity gradients in the meniscus and thus a large dissipation. Note that a similar behaviour is observed on a moving contact line for which the friction coefficient also displays a strong dependence upon the contact angle $\beta \sim 1/\theta$ [1].

In order to account for the experimental results, we developed a theoretical model for the oscillation of a liquid meniscus in cylindrical geometry (see SM). We consider the problem in the frame of reference attached to the cylinder (see Fig. 2). The flow induced by the interface motion leads to a friction coefficient β_{men} . The latter is related to the mean energy loss \mathcal{P} during an oscillation cycle, through $\mathcal{P} = \beta_{\text{men}}(A\omega)^2/2$ [17]. Since the capillary number is small – $Ca = A\omega\eta/\gamma \sim 10^{-3}$ – we may safely state that viscous effects do not affect the shape of the liquid interface. Therefore, the meniscus profile is solution of the Laplace equation resulting from the balance between capillary and hydrostatic pressures, which in turn yields the well known catenary shape [18–20]:

$$h = (R + r_0) \cos \theta \cosh \left(\frac{z}{(R + r_0) \cos \theta} - \ln(\zeta) \right), \quad (1)$$

were $\zeta = \cos \theta / [1 + \sin \theta]$. The meniscus height Z_0 is given, in the limit of small contact angles, by:

$$Z_0 = (R + r_0) \cos \theta \left[\ln \left(\frac{4 l_c}{R + r_0} \right) - \gamma_E \right], \quad (2)$$

with $\gamma_E \simeq 0.577$ the Euler constant and l_c the capillary length. Since $Z_0(t)$ oscillates around its mean position as $Z_0(\theta(t)) = Z_0(\bar{\theta}) + A \cos(\omega t)$, we can derive the temporal evolution of the contact angle:

$$\cos \theta(t) = \cos \bar{\theta} + \frac{A \cos(\omega t)}{(R + r_0) \left[\ln \left(\frac{4 l_c}{R + r_0} \right) - \gamma_E \right]}. \quad (3)$$

Note that our model is meant to deal with positive contact angles only, even if the defect thickness could in principle allow slightly negative ones. This defines a critical contact angle θ_{crit} related to the minimum value of $\bar{\theta}$ allowed by the model. One has: $\cos \theta_{\text{crit}} = 1 - A / [(R + r_0) (\ln(4 l_c / (R + r_0)) - \gamma_E)]$. This critical depinning angle on an ideally strong defect increases with respect to A and decreases with respect to $R + r_0$. The interface motion being known, the velocity field is derived using the Stokes equation. Indeed, gravity and inertia can be safely neglected ($Re \sim 10^{-8}$ and $l_c \simeq 2$ mm). Moreover, the viscous diffusion timescale $\tau_\nu = R^2/\nu$ is much smaller than the oscillation period ($\tau_\nu f \sim 10^{-7}$), such that the Stokes equation reduces to the simplest steady Stokes equation. Using the lubrication approximation, we have finally $\partial_z P = \eta \Delta_r v$ where P is the hydrodynamic pressure and v is the velocity component in the z direction. Finally, combining the mass conservation equation $-\partial_t(\pi h^2) + \partial_z q = 0$ – where q is the local flow rate through a liquid section of normal z , the no-slip (at $r = R$) and free interface (at $r = h$) boundary conditions, yields the velocity profile:

$$v(r, z, t) = \frac{2 [R^2 + 2 h^2 \ln(r/R) - r^2] \int_0^z du \partial_t(h^2)}{R^4 + 3 h^4 - 4 h^2 R^2 - 4 h^4 \ln(h/R)}. \quad (4)$$

From Eq. (4) we derive the expression of β_{men} :

$$\beta_{\text{men}}(\bar{\theta}) = \left\langle \frac{4\pi\eta}{A^2\omega^2} \int_0^{Z_0} \int_R^h (\partial_r v)^2 r dr dz \right\rangle_t, \quad (5)$$

where $\langle \rangle_t$ designates the temporal average over an oscillation cycle (see SM). Figure 2 displays an example of viscous stress field (color gradient) and velocity profile (vertical dark arrows) inside a nanomeniscus pinned on a defect with $r_0=40$ nm, for typical operating conditions. We observe that the stress is essentially localized at the fiber wall and strongly decays when z becomes of the order of a few probe radii. Hence, the lubrication approximation – only valid for small depths and small surface gradients ($\partial_z h \ll 1$) – is strengthened. When the mean contact angle $\bar{\theta}$ is decreased a strong increase of the viscous stress is observed but its localization remains mostly

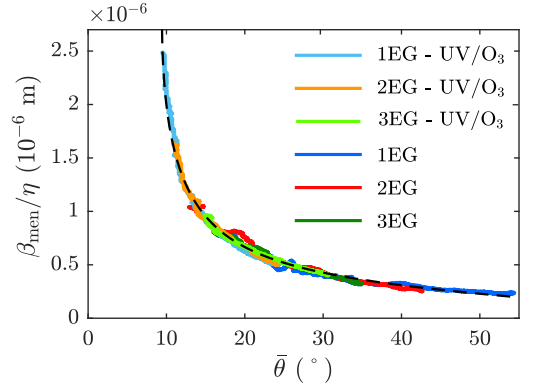


FIG. 3. Normalized friction coefficient β_{men}/η plotted as a function of $\bar{\theta}$ [see Eq. (5)]. The dashed line signifies the theoretical model, while the experimental dotted curves are performed over all the studied liquids, before and after UV/O₃ treatment, with $R=85$ nm, $A=18$ nm and $r_0=40$ nm.

unchanged (see SM). A striking result is the influence of the defect size. For contact angles close to the critical one, reduction in size of the defect increases significantly the viscous stress in a region closer to the contact line (see SM). Figure 3 displays an example of normalized friction coefficient curve β_{men}/η (dashed line), plotted as function of $\bar{\theta}$. A significant increase of β_{men} is observed for decreasing contact angles in agreement with the experimental observations.

To quantitatively confront the FM-AFM experiments to the theoretical model, we use the force signal to determine the experimental contact angles $\bar{\theta}$. We assume that, due to the inhomogeneous thickness of the platinum rings, the meniscus depins from the defect for a contact angle θ_{break} larger than θ_{crit} value expected for an ideal defect. The maximum force before depinning then reads $F_{\text{max}} = 2\pi\gamma(R + r_0) \cos \theta_{\text{break}}$ which allows to calculate the experimental contact angle for any d values using $\cos \bar{\theta} = [F/F_{\text{max}}] \cos \theta_{\text{break}}$. The latter equation enables to determine the contact angle for each d position without using the cantilever stiffness only known within 20 % error. For each experiment, we make a linear fit of the whole friction coefficient curve without taking into account the regions influenced by the defects. The subtraction of this fit allows to dispose of the viscous layer contribution, leaving only β_{men} and a constant term induced by the bottom of the tip, called β_{bottom} . The data are then fitted by computing the parameters β_{bottom} and θ_{break} which minimise the standard deviation between the experimental data and the theoretical curve [Eq. (5)]. As for R and r_0 , we use effective values measured by SEM. FM experiments were then performed over all the studied liquids. More than ninety experiments were carried out with two different home-made probes ($R = 80$ nm and 85 nm), defect thicknesses r_0 between 10 and 50 nm and oscillation amplitudes A ranging from 5 to 35 nm. Additionally, experiments were performed before and af-

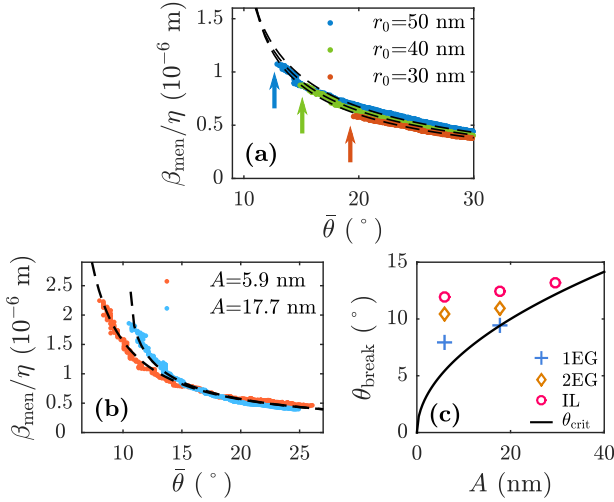


FIG. 4. (Normalized friction coefficient β_{men}/η vs mean contact angle $\bar{\theta}$ for different operating conditions. The dashed lines are plots of the theoretical model [Eq. (5)]. (a) Influence of ring thickness r_0 . The arrows indicate the value of θ_{break} . (b) Influence of oscillation amplitude A . (c) Plot of θ_{break} (symbols) and θ_{crit} (solid line) as a function of the oscillation amplitude for a defect of thickness $r_0 = 40$ nm.

ter surface cleaning by UV/O₃ treatment to assess the influence of tip wettability.

As an example, Fig. 3 displays six curves performed with three different liquids, before and after UV/O₃ treatment, on the same defect ($R = 85$ nm and $r_0 = 40$ nm) with an amplitude $A = 18$ nm. The agreement between the experimental data and the theoretical model is remarkable. A ten-fold enhancement of dissipation is observed when the contact angle is decreased from 50° to 10° . As expected, the five minute surface cleaning does not affect the dissipation process since all curves superpose on a same master curve. Yet, ozone cleaning has a strong impact on the θ_{break} values. The hydrophilic surfaces obtained after UV/O₃ treatment lead to a strong pinning which allows to reach smaller contact angle values. For example, for 1EG θ_{break} decreases from 18.5° to 9.5° , the latter value being very close from the value of $\theta_{\text{crit}} = 9.4^\circ$. Consequently, the dissipation can reach larger values after ozone treatment. This is a common observation on all the measurements. When the tip is more hydrophobic, the liquid may detach between the dots forming the defect before the θ_{crit} value is reached. In order to discuss further the influence of the various parameters and the resulting values of the fitting variables θ_{break} and β_{bottom} , we reported on Figure 4 a comparison between the theoretical model and FM experiments performed on 3EG for (a) different defect thicknesses and (b) various oscillation amplitudes. Figure 4(a) shows that the ring thickness r_0 has a low impact on the friction coefficient curve for $30 \text{ nm} \leq r_0 \leq 50 \text{ nm}$. Nevertheless, a systematic evolution of θ_{break} is observed: larger defect

thicknesses lead to a stronger pinning of the defect which results in a smaller θ_{break} value, as marked by the arrows on the curves. We also found that the oscillation amplitude only plays a significant role for contact angles close to θ_{crit} . Therefore its influence can only be noticed after the UV/O₃ treatment. The theoretical model reproduces well the influence of amplitude observed for contact angles smaller than 15° [see Fig. 4(b)]. A larger amplitude increases slightly the value β_{men} at low $\bar{\theta}$ and also leads to an increase of the θ_{break} value, a general trend observed on all experiments. On hydrophilic tips [see Fig. 4(c)], θ_{break} approaches the θ_{crit} value expected for an ideal defect, but dynamic effects are also probably involved since an effect of the liquid nature is observed.

The limited influence of the experimental parameters on the dissipation in the meniscus justifies reporting all the experimental results on a same curve (see SM) showing a general trend well reproduced by the model using two adjustable parameters. As expected, contrary to θ_{break} , β_{bottom} does not show any systematic influence of amplitude, defect size and wettability. Statistics over all experiments (see histogram in SM) show that β_{bottom} is proportional to the liquid viscosity and lead to $\beta_{\text{bottom}}/(\eta R) = 7 \pm 3.5$. If we assimilate the cylinder bottom to a disk of radius R , the dissipation induced by the fibre bottom is given by $\beta_{\text{bottom}} = 8\eta R$ (see ref. [21]), consistent with the experimental results. However, quantitative comparison with the theory is compromised due to the ill-defined shape of the tip end.

In conclusion, the development of dedicated AFM probes with defects of controlled size down to nanometer scale, combined with the use of frequency-modulation AFM, enables the accurate investigation of the viscous dissipation in anchored oscillating menisci. We find an excellent agreement between the experimental results and our lubrication based theoretical model describing the flow pattern inside the oscillating meniscus. The stretching of the meniscus leads to a strong increase of viscous stress which accounts for the surge of dissipated energy observed at small angle. Note that this effect is amplified for small defect sizes, in which case the stress is strongly localised at the contact line with important consequences on the wetting dynamics on surfaces with defects. Our results also give new insights on the depinning of the contact line from defects which appears for a contact angle value θ_{break} larger than the theoretical one θ_{crit} obtained for a perfect pinning. The latter value could be approached using hydrophilic tips showing that the pinning is all the stronger that the oscillation amplitude A is small and the defect size r_0 is large. This study demonstrates that FM-AFM is a unique tool for quantitative measurements of dissipation in confined liquids, down to the nanometer scale, and paves the way for a systematic study of open questions in wetting science regarding the extra dissipation which occurs when the contact line starts to move.

ACKNOWLEDGMENTS

The authors thank P. Salles for his help in the development of tip fabrication procedures, Dominique Anne-Archard for viscosity measurements and J.-P. Aimé, D. Legendre and E. Raphaël for fruitful discussions. This study has been partially supported through the ANR by the NANOFLUIDYN project (grant n° ANR-13-BS10-0009).

-
- [1] P. G. de Gennes, Rev. Mod. Phys. **57**, 827 (1985).
 - [2] D. Bonn, J. Eggers, J. Indekeu, J. Meunier, and E. Rolley, Rev. Mod. Phys. **81**, 739 (2009).
 - [3] J. H. Snoeijer and B. Andreotti, Ann. Rev. Fluid Mech. **45**, 269 (2013).
 - [4] J. Joanny and P.-G. De Gennes, J. Chem. Phys. **81**, 552 (1984).
 - [5] H. Perrin, R. Lhermerout, K. Davitt, E. Rolley, and B. Andreotti, Phys. Rev. Lett. **116**, 184502 (2016).
 - [6] X. Noblin, A. Buguin, and F. Brochard-Wyart, Eur. Phys. J. E **14**, 395 (2004).
 - [7] G. Michel, F. Pétrélis, and S. Fauve, Phys. Rev. Lett. **116**, 174301 (2016).
 - [8] T. Fukuma, Science and Technology of Advanced Materials **11**, 033003 (2010).
 - [9] A. Maali, T. Cohen-Bouhacina, and H. Kellay, Appl. Phys. Lett. **92**, 053101 (2008).
 - [10] J. Dupré de Baubigny *et al.*, Phys. Rev. Fluids **1**, 044104 (2016).
 - [11] S. Guo *et al.*, Phys. Rev. Lett. **111**, 026101 (2013).
 - [12] J. R. Vig, J. Vac. Sci. Technol. A **3**, 1027 (1985).
 - [13] F. J. Giessibl, Rev. Mod. Phys. **75**, 949 (2003).
 - [14] M. Delmas, M. Monthieux, and T. Ondarçuhu, Phys. Rev. Lett. **106**, 136102 (2011).
 - [15] A. H. Barber, S. R. Cohen, and H. D. Wagner, Phys. Rev. Lett. **92**, 186103 (2004).
 - [16] M. M. Yazdanpanah *et al.*, Langmuir **24**, 13753 (2008).
 - [17] J.-P. Pérez, *Mécanique: fondements et applications: avec 300 exercices et problèmes résolus* (Dunod, 2001).
 - [18] B. Derjaguin, Dokl. Akad. Nauk SSSR **51**, 517 (1946).
 - [19] D. F. James, J. Fluid Mech. **63**, 657 (1974).
 - [20] J. Dupré de Baubigny *et al.*, Langmuir **31**, 9790 (2015).
 - [21] W. Zhang and H. A. Stone, J. Fluid Mech. **367**, 329 (1998).

Supplemental material

Dynamics of an anchored oscillating nanomenisci

Caroline Mortagne,^{1,2} Kévin Lippera,^{1,3} Philippe Tordjeman,² Michael Benzaquen,³ Thierry

Ondařuhu¹

¹ *Nanosciences group, CEMES-CNRS, 29 rue Jeanne Marvig,
31055 Toulouse Cedex 4 France*

² *IMFT - Université de Toulouse, CNRS-INPT-UPS, 1 allée du Professeur Camille Soula,
31400 Toulouse France*

³ *LadHyX - Ecole Polytechnique, CNRS, Boulevard des Maréchaux,
91120 Palaiseau, France*

SM1: Tip fabrication	p. 2
SM2: Velocity profile and friction coefficient	p. 4
SM3: Flow patterns in the meniscus	p. 7
SM4: Master curve and statistics	p. 9

SM1: Tip fabrication

A two-step process was developed to fabricate the non-conventional tips used in this study.

In a first step (Fig. S1), a nanofiber is milled from a conventional AFM tip (OLTESPA-R3, Bruker) using a dual beam FIB (1540 XB Cross Beam, Zeiss). The initial pyramidal tip is progressively cut by slices of 100 to 500 nm width in order to keep only the front edge of the pyramid. It results in a fiber with a rounded triangular profile. Note that, for the comparison between the experimental results and the theoretical model based on a cylindrical geometry, we use an effective theoretical radius which gives the same perimeter as the actual tip. Radius as small as 25 nm can be fabricated but, in this study, we used tips of 80 nm or 85 nm radius, which are large enough to accommodate enough defects.

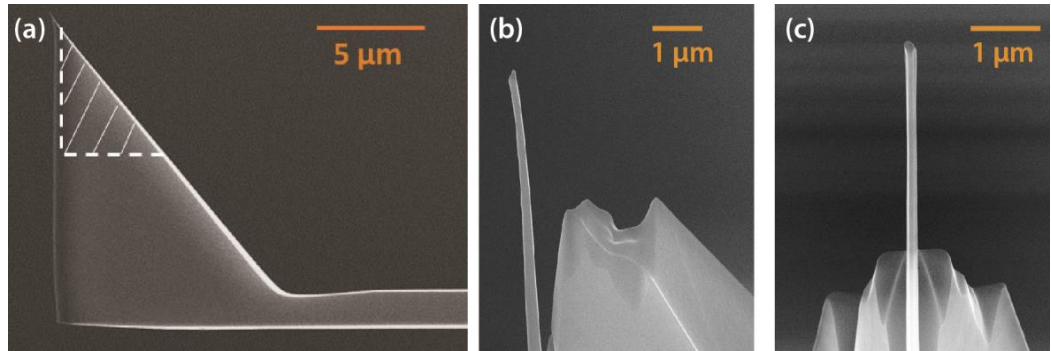


Figure S1: (a) Lateral SEM image of a OLTESPA-R3 (Bruker) tip. The hatched area represent the zone removed by FIB to carve the nanofiber; (b) – (c) Lateral and face view of a nanofiber after milling.

In a second step, defects are built on the nanofiber in order to pin the meniscus. This is achieved by Electron Beam Induced Deposition (EBID) using an ELPHY MultiBeam (Raith) and the gas injection system of the FIB. A platinum precursor gas injected close to the tip is decomposed by the electron beam, leaving platinum on the tip. Regular annular defects can not be achieved because a continuous motion of the electron beam results in a deposit which does not stick to the tip surface but rather forms a needle perpendicular to the tip. In order to solve

this issue, discontinuous defects are built, as shown in Figure S2. Spots with diameter ranging from 10 nm to 40 nm can be achieved. The distance between spots was adjusted in order to get the closest possible spots. Interestingly, due to the partial transparency of the thin nanofibers to electrons, thinner defects are also deposited on the back side of the tip. As a consequence of the annular defect inhomogeneity, the contact line can depin for a contact angle θ_{break} larger than the theoretical value θ_{crit} . Note that the defects rings form an angle of 11° with respect to the perpendicular to the tip axis in order to compensate for the inclination of the tip in the AFM head and insuring that the defect is perpendicular to the liquid interface.

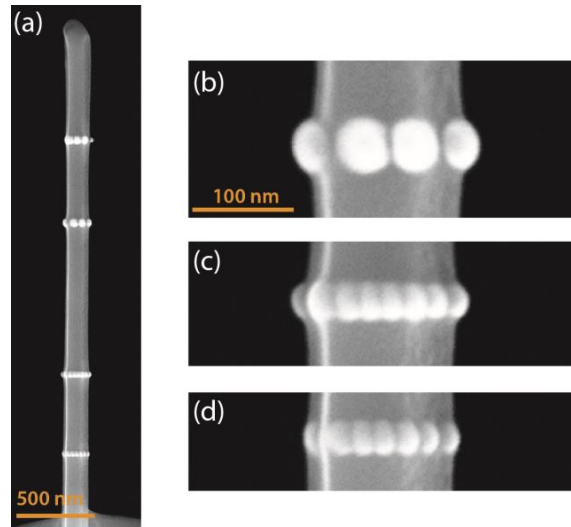


Figure S2: (a) SEM image of the same tip as in Fig. SM1 with 4 rings of defects deposited by EBID; (b) – (d) Zooms on the three lower defects.

SM2: Velocity profile and friction coefficient

We consider the flow induced by the interface motion of a liquid meniscus anchored on a cylinder rod, of radius R , oscillating along its axis, z . The meniscus contact line is pinned on an annular topographical defect of radius r_0 . In the frame of reference attached to the cylinder, the velocity field is solution, for a purely viscous Newtonian liquid under the lubrication approximation, of the Stokes equation

$$\partial_z P = \eta \Delta_r v, \quad (\text{SI1})$$

where P is the hydrodynamic pressure, η is the fluid viscosity and v is the velocity component in the z direction. Equation (SI1), together with a no-slip boundary condition at the rod's surface, at $r = R$, and a no-stress boundary condition at the free interface, at $r = h(z)$, relates the velocity field to the hydrodynamic pressure gradient through the equation:

$$v(r, z) = \frac{\partial_z P(z) \left(r^2 - 2h^2(z) \ln\left(\frac{r}{R}\right) - R^2 \right)}{4\eta}. \quad (\text{SI2})$$

Furthermore, the velocity field is related to the interface profile through the mass conservation equation

$$\partial_t(\pi h^2) + \partial_z \int_R^{h(z)} dr v(r, z) r = 0. \quad (\text{SI3})$$

From Eq. (SI3) we derive the pressure gradient inside the meniscus

$$\partial_z P(z) = - \frac{8\eta \int_0^z du \partial_t(h^2)}{R^4 + 3h^2 - 4h^2 R^2 - 4h^4 \ln\left(\frac{h}{R}\right)}, \quad (\text{SI4})$$

which, in turns, gives the velocity profile as a function of the interface profile

$$v(r, z) = \frac{2 \left(R^2 + 2h^2 \ln\left(\frac{r}{R}\right) - r^2 \right) \int_0^z du \partial_t(h^2)}{R^4 + 3h^2 - 4h^2 R^2 - 4h^4 \ln\left(\frac{h}{R}\right)}. \quad (\text{SI5})$$

Since the capillary number is small ($Ca = A \omega \eta / \gamma \sim 10^{-3}$) we assume that viscous effects do not affect the shape of the liquid interface. The meniscus profile is therefore solution of the Laplace equation resulting from the balance between capillary and hydrostatic pressures, which yields the well-known catenary shape

$$h(z) = (R + r_0) \cos \theta \cosh \left(\frac{z}{(R + r_0) \cos(\theta)} - \ln \left[\frac{\cos(\theta)}{1 + \sin(\theta)} \right] \right), \quad (\text{SI6})$$

where θ is the wetting contact angle of the meniscus.

As the contact line is pinned during the rod oscillation, the meniscus height, $Z_0(\theta)$, oscillates around its mean position, $Z_0(\bar{\theta})$, with $Z_0(\theta[t]) = Z_0(\bar{\theta}) + A \cos(\omega t)$, where $\bar{\theta}$, A and ω are respectively the mean contact angle, the amplitude and the angular frequency of the oscillation. Together with the expression of $Z_0(\theta)$, which reads for small contact angle

$$Z_0(\theta) = (R + r_0) \cos \theta \left[\ln \left(\frac{4l_c}{R + r_0} \right) - \gamma_E \right], \quad (\text{SI7})$$

we derive thus the temporal evolution of the contact angle

$$\cos \theta = \cos \bar{\theta} + \frac{A \cos(\omega t)}{(R + r_0) \left[\ln \left(\frac{4l_c}{R + r_0} \right) - \gamma_E \right]}. \quad (\text{SI8})$$

Hence, Eqs. (SI5), (SI6) and (SI8) give the velocity profile inside the meniscus. Note that our model is meant to deal with positive contact angles only, even if the defect thickness could in principle allow slightly negative ones. From Eq. (SI8) we obtain therefore a critical contact angle, θ_{crit} , corresponding to the minimum value of $\bar{\theta}$ allowed by the model, with

$$\cos \theta_{crit} = 1 - \frac{A}{(R + r_0) \left[\ln \left(\frac{4l_c}{R + r_0} \right) - \gamma_E \right]}. \quad (\text{SI9})$$

We can now determinate the friction coefficient associated with the meniscus, β_{men} . For a forced harmonic oscillator that dissipates energy through viscous damping, the mean energy loss during an oscillation cycle, P , is related to the friction coefficient through the relation

$$P = \frac{\beta_{men} (A\omega)^2}{2}. \quad (\text{SI10})$$

Furthermore, P is given, for a viscous Newtonian liquid under lubrication approximation, by

$$P = \left\langle \eta \oint_V (\partial_r v)^2 dV \right\rangle_t, \quad (\text{SI11})$$

where $\langle \rangle_t$ designates the temporal average over an oscillation cycle. Combining Eqs. (SI10) and (SI11) we obtain

$$\beta_{mean} = \left\langle \frac{2\eta}{(A\omega)^2} \oint_V (\partial_r v)^2 dV \right\rangle_t. \quad (\text{SI12})$$

The case of small amplitude

We consider the asymptotic limit of small oscillation amplitude where $\sin\theta(t) \simeq \sin\bar{\theta}$ and $h(\theta(t)) \simeq h(\bar{\theta})$. Under this approximation, the derivative of the contact angle $\dot{\theta}$ reads

$$\dot{\theta}(t) \simeq \frac{A \sin(\omega t)}{\sin\bar{\theta}(R + r_0) \left[\ln\left(\frac{4l_c}{R + r_0}\right) - \gamma_E \right]}, \quad (\text{SI13})$$

and the normalized viscous stress is given by the equation

$$\partial_r v \simeq \frac{4\dot{\theta}(h^2/r - r) \int_0^{h(z)} du \partial_{\bar{\theta}}(h^2)}{R^4 + 3h^2 - 4h^2 R^2 - 4h^4 \ln\left(\frac{h}{R}\right)} = A \tilde{\sigma}_{rz}, \quad (\text{SI14})$$

where we introduce $\tilde{\sigma}_{rz}(r, z, \bar{\theta}) = \frac{4 \sin(\omega t) \left(\frac{h^2}{r} - r\right) \int_0^{h(z)} du \partial_{\bar{\theta}}(h^2)}{\sin\bar{\theta}(R + r_0) \left[\ln\left(\frac{4l_c}{R + r_0}\right) - \gamma_E \right] (R^4 + 3h^2 - 4h^2 R^2 - 4h^4 \ln\left(\frac{h}{R}\right))}$. Since $\partial_r v$

is proportional to the amplitude A , we obtain from Eq. (SI12) that β_{mean} does not depend on A in the asymptotic case of small amplitude. However, the Taylor expansion of Eq. (SI9) shows that the critical contact angle, θ_{crit} , varies as the square root of A with

$$\theta_{crit} = \sqrt{\frac{2A}{(R + r_0) \left[\ln\left(\frac{4l_c}{R + r_0}\right) - \gamma_E \right]}}. \quad (\text{SI15})$$

SM3: Flow patterns inside the meniscus

The hydrodynamic model described in the paper provides a comprehensive description of flow patterns in an oscillating nanomeniscus which lead to the measured friction coefficient. The flow is mainly influenced by two parameters: the mean contact angle $\bar{\theta}$ and the defect size r_0 , whose influence are discussed below.

- **Influence of the mean contact angle $\bar{\theta}$**

In Fig. S3 are reported the viscous stress field inside the meniscus as the mean contact angle $\bar{\theta}$ is reduced from $\bar{\theta} = 22^\circ$ down to $\bar{\theta} = \theta_{crit} = 6.73^\circ$ which is the depinning contact angle associated with the conditions used in the calculation, namely $r_0 = 40$ nm and $A = 10$ nm. The maximum stress is obtained at the fiber surface at a distance of about $2.5 r_0$ from the contact line. The decrease of contact angle significantly increases the value of the stress without any noticeable modification of the position of its localization inside the nanomeniscus.

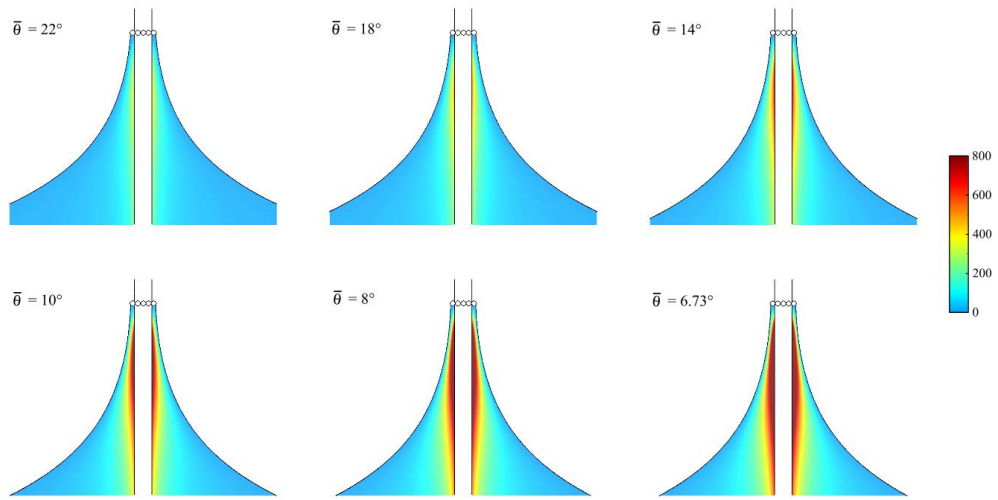


Figure S3: Viscous stress field $\eta \partial_r v$ (color gradient), computed at $t = 0$, for 6 different contact angles and $R = 100$ nm, $r_0 = 30$ nm, $l_c = 2$ mm, $A = 10$ nm, $f = 65$ kHz and $\eta = 30$ mPa.s. Color bar in Pa.

- **Influence of the defect size**

The defect height r_0 has a strong influence on the dissipation pattern as shown in Fig. S4. A decrease of defect size leads to a strong enhancement of the viscous stress inside the meniscus, which can be understood by the fact that small defects results in smaller films thickness at the contact line and consequently larger velocity gradients. Another striking effect is that the defect size also affects the localization of the viscous field which becomes concentrated closer from the contact line as r_0 is decreased. This effects is not straightforward and may have important consequences on the wetting on surfaces with defects.

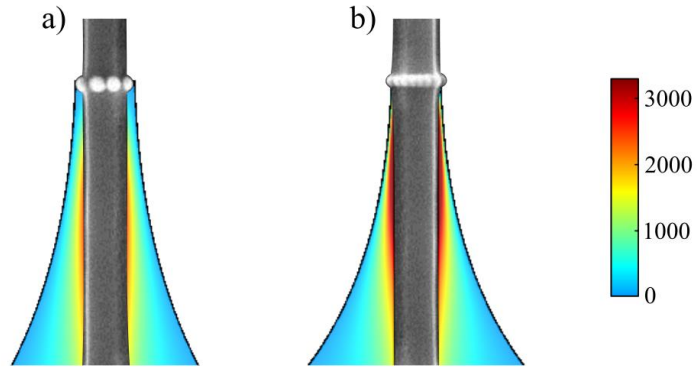


Figure S4: Viscous stress field $\eta \partial_r v$ (color gradient), computed at the critical contact angle value and $t = 0 \text{ s}$, for 2 different defect sizes : (a) $r_0 = 40 \text{ nm}$ and (b) $r_0 = 10 \text{ nm}$. The parameters used are $R = 100 \text{ nm}$, $l_c = 2 \text{ mm}$, $A = 10 \text{ nm}$, $f = 65 \text{ kHz}$ and $\eta = 30 \text{ mPa.s}$. Color bar in Pa.

SM4: Master curve and statistics

As shown in the paper, the experimental conditions, namely the defect size r_0 and the oscillation amplitude A , have a small influence on the friction coefficient. We therefore reported in Fig. SM5 around twenty curves performed using different tips, defects, liquids and amplitude. All curves superpose in a rather thin zone which is nicely bounded by the theoretical curves giving the extreme cases within the range of experimental conditions ($10 \text{ nm} \leq r_0 \leq 50 \text{ nm}$ and $6 \text{ nm} \leq A \leq 33 \text{ nm}$). The higher dissipation is obtained for small defect and high amplitude ($r_0 = 5 \text{ nm}$ and $A = 33 \text{ nm}$).

From all the measurements (more than ninety), we extracted a histogram of the values of β_{bottom} used in the fits (inset Fig. S5). The mean value of $\beta_{bottom} = (7 \pm 3.5)\eta R$ is consistent with the theoretical expression, $\beta_{bottom} = 8\eta R$, expected for a flat tip end. However, the ill-defined tip end geometry leads to a strong dispersion of the experimental results which hinders a more quantitative comparison with the theory.

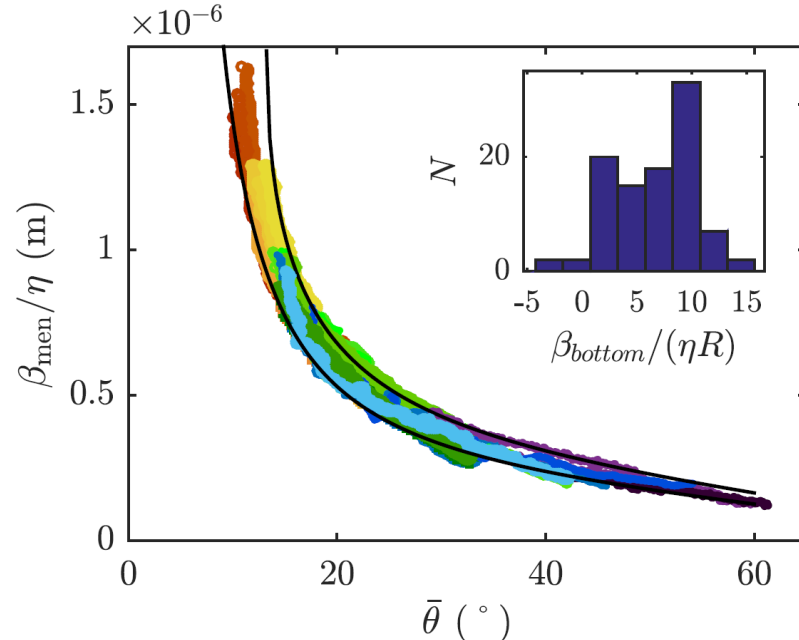


Figure S5: (a) Superposition of all the experimental curves. In order to visualize different curves, the color is related to the θ_{break} value. The range of theoretical values appears in

grey and is limited by two solid lines ($r_0 = 5 \text{ nm}$, $A = 33 \text{ nm}$ for the higher one and $r_0 = 50 \text{ nm}$, $A = 6 \text{ nm}$ for the lower one); (b) Histogram of the $\beta_{bottom}/\eta R$ values extracted from the experimental data.